Soft Matter

PAPER

# Structural rheology of focal conic domains: a stress-quench experiment†

Cite this: *Soft Matter*, 2014, **10**, 5289

Shuji Fujii,[a] Shigeyuki Komura*[b] and C.-Y. David Lu[c]

Received 19th January 2014
Accepted 28th April 2014

DOI: 10.1039/c4sm00146j

www.rsc.org/softmatter

We study the dynamics of focal conic domain (FCD) formation in a thermotropic smectic phase under shear stress. It is known that increasing the shear stress induces a non-equilibrium phase transition from a smectic phase with FCDs ($SmA_I$) to another smectic phase ($SmA_{II}$) in which the layers are oriented. By quenching the shear stress from the $SmA_{II}$ phase to the $SmA_I$ phase, we find three characteristic modes in the FCD formation process. The first mode is attributed to the edge dislocation dynamics induced by climb motions. The second mode results from FCD formation. The first and second modes show slowing down close to the smectic–nematic transition temperature, implying that the dynamics are dominated by dislocation unbinding. The third mode originates from the alignment of FCDs which form oily streaks. Such an alignment occurs when the shear stress balances the line tension of the oily streaks.

## 1 Introduction

When shear flow is applied to a smectic phase, non-equilibrium dislocations and textural defects such as focal conic domains (FCDs) are formed, which significantly influence the smectic rheology.[1–12] Defect-mediated rheology in the smectic phase is an important issue in structural rheology, which deals with the flow properties influenced by meso-scale structures in soft matter.[13]

Defects and dislocations affect both rheological responses and dynamic phase behaviors of soft matter.[14] Fig. 1 shows a dynamic orientation diagram of 4-*n*-octyl-4′-cyanobiphenyl (8CB) thermotropic liquid crystals obtained by the present authors.[9] The smectic phase is divided into two types; the $SmA_I$ phase in which the sample is occupied by micrometer-scale FCDs, and the $SmA_{II}$ phase characterized by perpendicularly oriented smectic layers.[9,15,16] At constant temperature, the $SmA_I$ phase converts to the $SmA_{II}$ phase by increasing the shear stress $\sigma$. Shear stress induces a layer orientation transition, which is not observed at equilibrium.[15,16] In the vicinity of the equilibrium smectic–nematic transition temperature $T_{SN}$, the $SmA_{II}$ phase can be easily formed by the shear stress, and decreasing the temperature expands the region of the $SmA_I$ phase. Appearance of the $SmA_{II}$ phase and the increased FCD size around $T_{SN}$ are intimately related through the dislocation unbinding mechanism.[9,17] Shear stress dependence of the FCD size and layer orientation in the dynamic phase diagram reflect the observed shear-thinning behavior.[9]

Although various non-equilibrium phases and structural transitions in soft matter have been extensively investigated,[2,18,19] the relationship between the structural transition

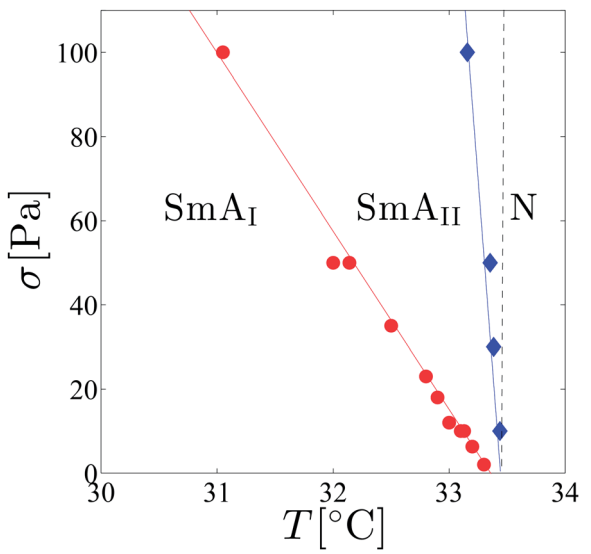


Fig. 1 Dynamic orientation diagram of 8CB under shear stress as a function of temperature $T$ and applied shear stress $\sigma$, reproduced from ref. 9. "$SmA_I$" and "$SmA_{II}$" denote the smectic phases with FCDs and perpendicularly oriented smectic layers without FCD, respectively, and "N" indicates the nematic phase. The vertical dashed line indicates the smectic–nematic transition temperature $T_{SN} = 33.4$ °C.

[a]*Department of Chemistry, Nagaoka University of Technology, Nagaoka 940-2188, Japan. E-mail: sfujii@mst.nagaokaut.ac.jp*

[b]*Department of Chemistry, Tokyo Metropolitan University, Tokyo 192-0397, Japan. E-mail: komura@tmu.ac.jp*

[c]*Department of Chemistry, National Taiwan University, Taipei 106, Taiwan. E-mail: cydlu@ntu.edu.tw*

† Electronic supplementary information (ESI) available: Stress quench data obtained by a cone-plate shear cell made of stainless steel and a parallel plate shear cell made of quartz are compared. Spatio-temporal images used for the construction of Fig. 6 and 7 are also shown. See DOI: 10.1039/c4sm00146j

and the rheological behavior is inadequately understood. Especially, the kinetic pathway between different non-equilibrium phases remains unsolved because few experimental data have been published.[20,21] In this paper, we perform a stress-quench experiment to elucidate the non-equilibrium FCD formation in a thermotropic smectic phase. Specifically, we investigate the temporal mechanical response of the dynamical transition during sudden quenching of the shear stress from the $SmA_{II}$ phase to the $SmA_{I}$ phase.

In lyotropic systems, it is known that multilamellar vesicles (onions) are formed by applying a shear flow to a lamellar phase, and the onion size depends on the shear rate.[22] Recently, one of the authors studied the growth of the onion structure by a shear-quench experiment.[23,24] We found that the transition pathway can be either continuous or discontinuous depending on the quench depth of the shear rate. During discontinuous transitions, onions dissociate into planar lamellae in two steps, and new onions of different sizes are formed. Notably, FCDs and onions belong to the same class of defect, but their Gaussian curvatures differ.[25] In fact, the elasticity of FCDs and onions depends on the effective surface tension of the layered systems.[10] Hence, the non-equilibrium transitions of FCDs and onions are expected to share some similar features.

Section 2 of this paper describes our shear stress-quench method and tested materials. In Section 3, we explain our experimental results for different temperatures, and show that FCD formation is characterized by three distinctive dynamical modes. Possible physical origins of these modes are proposed in Section 4. Section 5 summarizes our findings.

## 2 Experiment

We used the thermotropic liquid crystal 4-*n*-octyl-4′-cyanobiphenyl (8CB). 8CB was purchased from Synthon Chemicals GmbH Co., Germany and was used without further purification. The equilibrium phase sequence and the rheological property of 8CB have been well characterized in the literature.[9,10,15,16] Rheological measurements were performed using a stress-controlled rheometer, Anton Paar MCR-300, equipped with a truncated cone-plate (made of stainless steel). The diameter and the cone angle were 50 mm and 0.017 rad, respectively.

Microscopy observation under shear flow was performed using a polarized microscope attached to another rheometer, Anton Paar MCR-501, with a parallel plate (made of quartz). The diameter of the quartz shear cell was 50 mm, and the sample thickness was fixed to 150 μm. Incident light was polarized along the flow direction, and the analyzer was aligned perpendicular to the flow direction. This setup enables simultaneous measurement of the viscosity and the structure under crossed-nicols. We confirmed that the rheological data obtained by MCR-300 and MCR-501 qualitatively coincide (see Fig. S1 of the ESI†).

During the structural observation, the flow patterns were recorded as movies at a frame rate of 30 fps. The obtained movies were converted into spatio-temporal images using ImageJ. Here the optical intensity of a line of pixels along the vorticity direction (the left edge) of each frame was arrayed in a time-sequential order. Since the microscopy images were obtained under crossed-nicols, the optical intensity reflects the birefringence intensity. To evaluate the FCD density, the optical intensity at each time in the spatio-temporal image was averaged over 200 μm along the vorticity direction. As described in Fig. S2 and S3 of the ESI,† the position of the FCD was defined by the focal point of an ellipse (apex). Time evolution of the FCD positions in the vorticity direction was also extracted from the spatio-temporal images. These images directly reveal the density variation and the alignment behavior of FCDs.

Prior to each stress-quench experiment, the sample was pre-sheared under an initial shear stress $\sigma_i = 85$ Pa for 200 s. This is sufficiently long for the system to reach a steady state, and to eliminate the flow history effect generated by the sample loading processes. Once the system reached the steady state, the shear stress was suddenly decreased from $\sigma_i = 85$ Pa to a final value $\sigma_f$, and the resultant shear rate $\dot{\gamma}$ and the flow behavior were observed as a function of time $t$. The stress-quench experiment was repeated at different temperatures. Note that, at $\sigma_i = 85$ Pa, the system is in the $SmA_{II}$ phase over the temperature range $T = 31.5$–$33.2$ °C (see Fig. 1). Below $T = 31.5$ °C and $\sigma < 85$ Pa, the $SmA_{I}$ phase is filled with FCDs.

## 3 Results

Fig. 2(a) and (b) show time sequences of the snap shots after quenching the system from $\sigma_i = 85$ Pa to $\sigma_f = 0.1$ Pa at $T = 33.0$ °C and from $\sigma_i = 85$ to $\sigma_f = 1.5$ Pa at $T = 31.0$ °C. The brightness of the images reflects the birefringence intensity. The first image in Fig. 2(a) (at $t = 0$ s) is considerably bright because the smectic layer adopted a perpendicular orientation.[9,15,16] After the stress-quench, the optical intensity rapidly decreased within a few seconds. The relaxation of the intensity is caused by a flip of smectic layers from the perpendicular to parallel orientation. At approximately $t = 50$ s, FCDs appeared as parabolic structures,[26,27] and their number density increased over time. By contrast, the first image (at $t = 0$ s) in Fig. 2(b) reveals an inhomogeneous birefringence pattern imposed by FCDs. At later times, one can see parabolic patterns as well as circular objects, which are also FCDs with smaller sizes. The FCD size distribution changed over time as the population of larger FCDs increased. At approximately $t = 900$ s after the stress-quench, large FCDs aligned along the flow direction (oily streaks) appeared. The FCDs were smaller at $T = 31.0$ °C than at $T = 33.0$ °C, which is consistent with our previous result.[10]

Fig. 3 plots the measured shear rate $\dot{\gamma}$ as a function of time $t$ for stress-quenches at different temperatures (a) $T = 33.0$, (b) 32.0, (c) 31.0 and (d) 30.0 °C. The first mode, the initial decay of $\dot{\gamma}$, can be fitted by a single exponential function as explained below. When the system underwent the non-equilibrium phase transition, the shear rate exhibited the second decay mode, which accompanies FCD formation. As the final stress $\sigma_f$ decreased, the fraction of the second mode markedly increased. Interestingly, when the system was quenched within the $SmA_{I}$ phase at $T = 31.0$ and 30.0 °C (Fig. 3(c) and (d), respectively), the shear rate showed anomalous behavior depending on the stress-quench depth. As the quench depth increased, the two decay modes appeared, similar to those at $T = 33.0$ and 32.0 °C

 

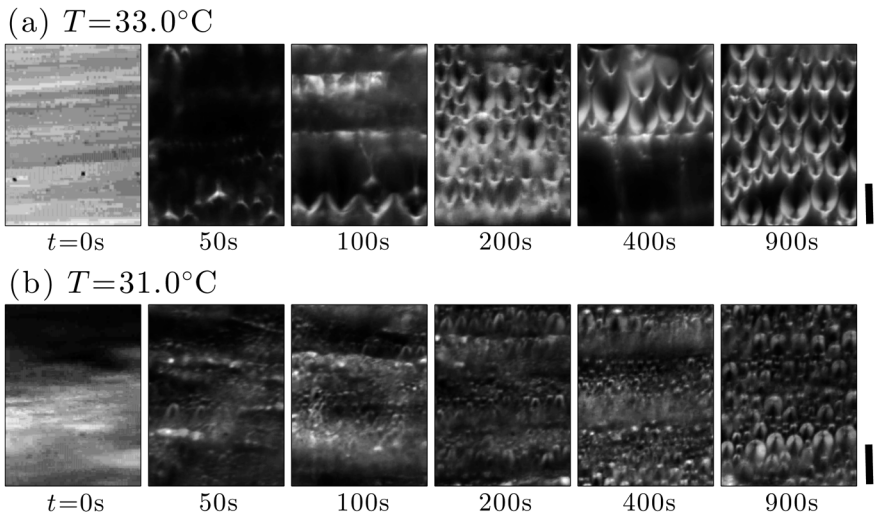


Fig. 2 Time sequence of polarized microscope images after quenching the system at (a) $T = 33.0$ °C and (b) $T = 31.0$ °C. Shear stress was quenched from $\sigma_i = 85$ Pa to $\sigma_f = 0.1$ Pa in (a) and from $\sigma_i = 85$ Pa to $\sigma_f = 1.5$ Pa in (b), respectively. The horizontal direction is the flow direction. The size of each image is 150 μm × 200 μm (the scale bars correspond to 50 μm). The brightness of these images reflects the birefringence intensity.

(Fig. 3(a) and (b), respectively). At lower temperatures, a third mode appeared during which the shear rate increased from its minimum. The third mode became more apparent as the temperature further decreased. In the following, we analyze these three modes more quantitatively and discuss their physical origins.

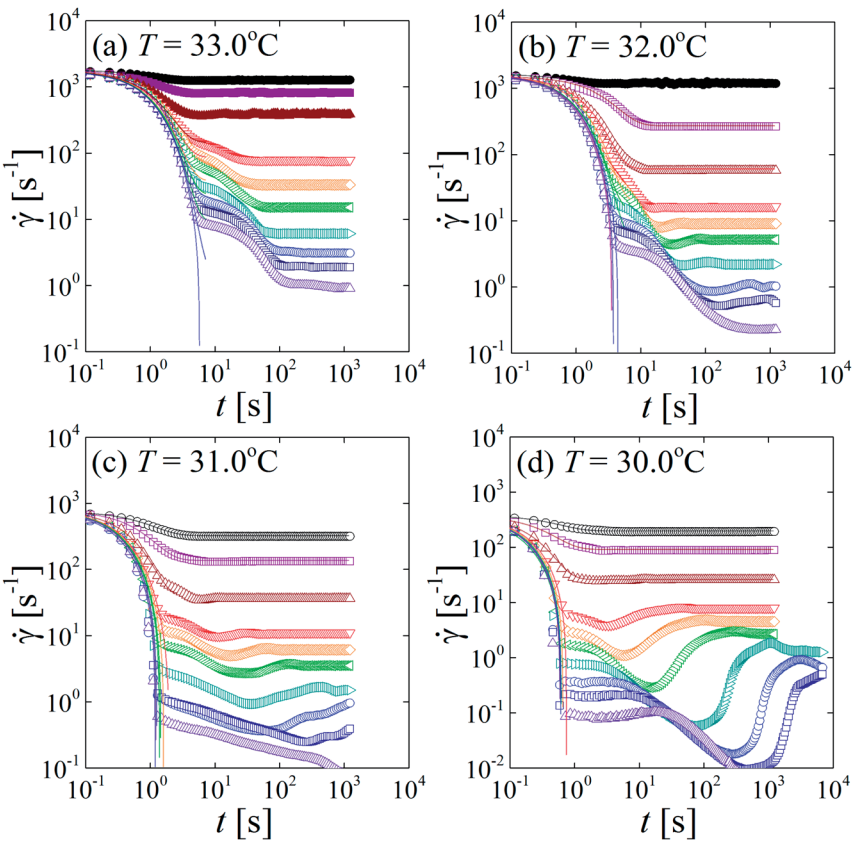


Fig. 3 Log–log plots of the measured shear rate $\dot{\gamma}$ as a function of the elapsed time $t$ after the stress-quench from $\sigma_i = 85$ Pa to $\sigma_f = 60$, 40, 20, 10, 7, 5, 3, 2, 1.5, 1 Pa (from upper to bottom) for (a) $T = 33.0$, (b) 32.0, (c) 31.0 and (d) 30.0 °C. The filled and the open symbols correspond to the stress-quench within the $SmA_{II}$ phase and from the $SmA_{II}$ to the $SmA_I$ phases, respectively. In (c) and (d), the stress-quench was applied within the $SmA_I$ phase only. Solid curves are the fits using a single exponential function with a characteristic time $\tau_1$ [see eqn (1)].

### 3.1 Formation of dislocations: first mode

As mentioned above, the first decay mode can be empirically fitted by a single exponential function

$$\dot{\gamma}(t) = \dot{\gamma}_0 \exp(-t/\tau_1), \quad (1)$$

where $\tau_1$ is the relaxation time. Fig. 4 plots $\tau_1$ as a function of $\sigma_f$ at different temperatures. We observe that $\tau_1$ levels off and becomes constant when $\sigma_f$ < 1 Pa. On the other hand, $\tau_1$ increases as the temperature approaches $T_{SN}$.

Fig. 5 plots the temperature dependence of $\tau_1$ at $\sigma_f = 1$ Pa. As $T_{SN}$ is approached from below, $\tau_1$ increases in two steps. At $\sigma$ = 85 Pa, the crossover temperature coincides with the boundary temperature ($T \simeq 31.3$ °C) between the $SmA_{II}$ and the $SmA_I$ phases. For $T > 31.3$ °C, the initial shear stress $\sigma_i = 85$ Pa is located inside the $SmA_{II}$ region, while it is within the $SmA_I$ phase for $T < 31.3$ °C. The increase of $\tau_1$ as a function of the reduced temperature, defined as $\varepsilon = (T_{SN} - T)/T$, obeys different power-law behaviors; $\tau_1 \sim \varepsilon^{-0.14\pm0.03}$ and $\tau_1 \sim \varepsilon^{-2.96\pm0.02}$, above and below $T = 31.3$ °C, respectively.

Since the smectic layers are perpendicularly oriented in the $SmA_{II}$ phase, the flip of the layers from the perpendicular to the parallel orientation accompanies a bending deformation. Accumulated stress of smectic layers as a result of the bending deformation can be relaxed by creation and proliferation of edge dislocations.[28] Under shear stress, these dislocations exhibit climb motion,[5–7,29] and reduce the shear rate by introducing their line tension. Note that edge dislocations drive the FCD dynamics, since they connect FCDs into oily streaks.[30] Later, we will attribute the first mode to the climb motion of edge dislocations.

### 3.2 Formation of FCDs: second mode

Fig. 6 shows the positions of FCDs extracted from the spatio-temporal images for the conditions described in Fig. 2. The spatio-temporal images under each quench condition are shown in Fig. S2 of the ESI.† The positions of FCDs at very short times are not shown because they were not easily determined in the unfocused images. Comparing Fig. 6(a) and (b), we recognize that the FCD density depends strongly on the temperature; FCDs are more dilute at a higher temperature and crowded at a lower temperature. As time progresses, FCDs gradually align along the flow direction.

Fig. 7 shows how the optical intensity of spatio-temporal images changes over time. These images were spatially averaged in the vertical direction (see Section 2). Again, the optical intensity reflects the number density of FCDs, because it is proportional to the birefringence intensity generated by FCDs. The characteristic time $\tau_2$ of the second mode was estimated by fitting the optical intensity to the empirical formula:

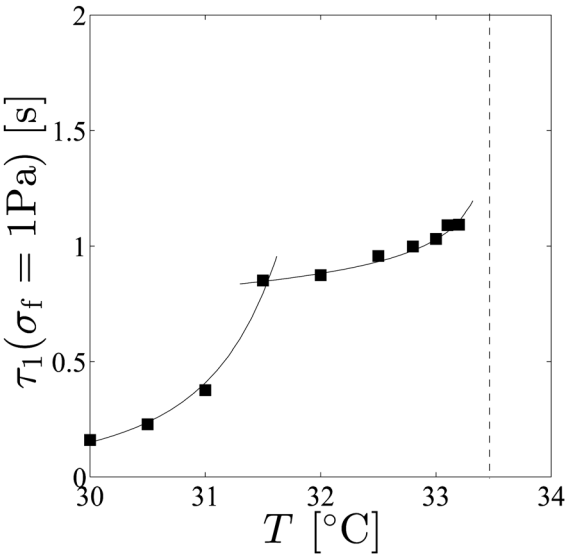


Fig. 5 Plot of $\tau_1$ at $\sigma_f = 1$ Pa as a function of temperature $T$ obtained from Fig. 4. Solid curves show $\tau_1 \sim \varepsilon^{-0.14\pm0.03}$ (right) and $\tau_1 \sim \varepsilon^{-2.96\pm0.02}$ (left), where $\varepsilon$ is the reduced temperature $\varepsilon = (T_{SN} - T)/T_{SN}$. The vertical dashed line indicates the smectic–nematic transition temperature $T_{SN}$ = 33.4 °C.

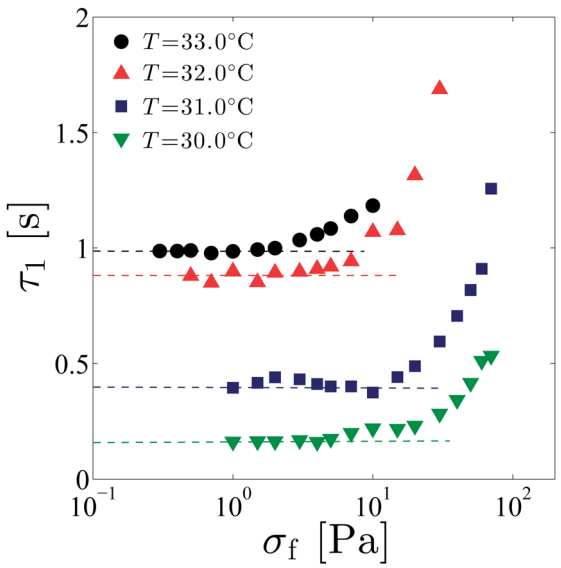


Fig. 4 Semi-log plot of $\tau_1$ as a function of $\sigma_f$ obtained from Fig. 3 for $T$ = 33.0, 32.0, 31.0, 30.0 °C. As indicated by the horizontal dashed lines, $\tau_1$ takes a constant value for small $\sigma_f$.

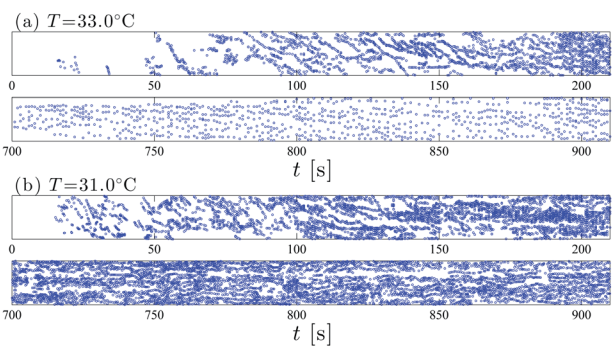


Fig. 6 Time evolution of FCD positions at (a) $T$ = 33.0 °C and (b) $T$ = 31.0 °C. The position of each FCD was defined by its focal point. The stress-quench condition is that described in Fig. 2.

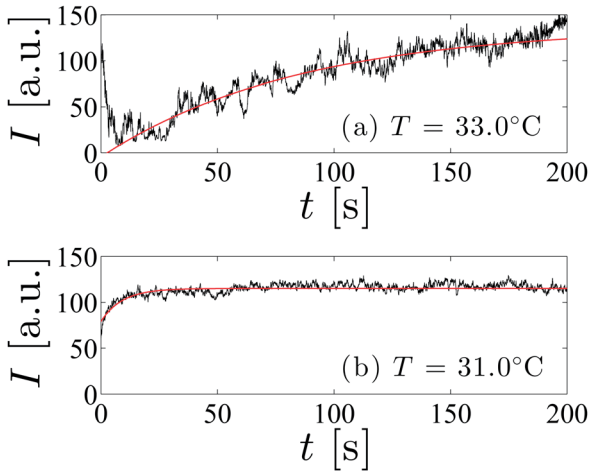


Fig. 7 Plot of averaged optical intensity $I$ as a function of time $t$ at (a) $T = 33.0$ °C and (b) $T = 31.0$ °C. Solid curves are the fits using a single exponential function with a characteristic time $\tau_2$ [see eqn (2)].

$$I(t) = I_0[1 - \exp(-t/\tau_2)]. \quad (2)$$

According to the rheological measurement, the obtained $\tau_2$ indeed corresponds to the second mode of the shear rate relaxation. Hence the present mode can be attributed to the formation of FCDs and their evolution to the densely packed configurations.

The temperature dependence of $\tau_2$ is plotted in Fig. 8. The shear stress dependence of $\tau_2$ was not investigated because of limited experimental data. We observed that $\tau_2$ increases as $T_{SN}$ is approached from below and obeyed a different power-law behavior; $\tau_2 \sim \varepsilon^{-1.03\pm0.02}$. Such slowing down behavior implied that FCD formation was influenced by a dislocation unbinding mechanism.[17]

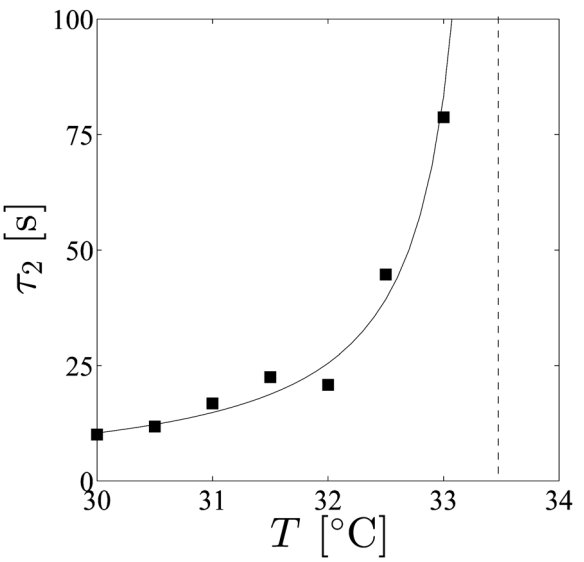


Fig. 8 Plot of $\tau_2$ as a function of temperature $T$. The solid curve is $\tau_2 \sim \varepsilon^{-1.03\pm0.02}$. The vertical dashed line indicates the smectic–nematic transition temperature $T_{SN} = 33.4$ °C.

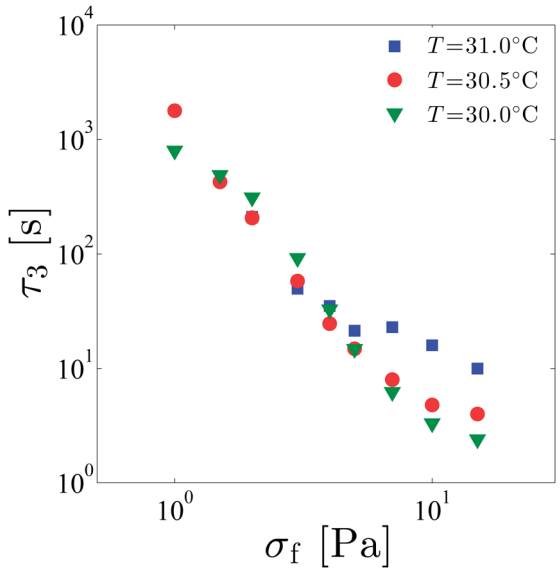


Fig. 9 log–log plot of $\tau_3$ as a function of $\sigma_f$ for different temperatures, $T = 31.0$, 30.5, 30.0 °C.

### 3.3 Alignment of FCDs: third mode

The third mode manifests as an increase in the shear rate (see Fig. 3(c) and (d)). Comparing Fig. 3 with Figs 2 and 6, the third mode is temporally consistent with the FCD alignment. Shortly after the stress-quench $t = 100$–200 s in Fig. 6(a), FCDs are not yet aligned along the flow direction. The alignment of FCDs occur at $t = 700$–900 s, following the shear rate decay. A similar ordering process is observed in Fig. 6(b). Hence, we attribute the third mode to the FCD alignment, *i.e.*, adjustment of oily streaks along the flow direction. Incidentally, a similar phenomenon was observed in the lane formation of colloidal dispersions under an electric field.[31]

We have characterized the third mode by $\tau_3$ when the shear rate took minimum values in Fig. 3. In Fig. 3(a) and (b), however, we did not determine $\tau_3$ because there was no minimum in the shear rate. Fig. 9 plots $\tau_3$ as a function of $\sigma_f$ at three different temperatures. Clearly, the alignment of FCDs depends on the final shear stress $\sigma_f$. The third mode $\tau_3$ significantly reduces as $\sigma_f$ increases, leveling off at high $\sigma_f$. Since oily streaks consisted of FCDs connected by edge dislocations,[30] the FCD alignment could be influenced by the dislocation unbinding. However, $\tau_3$ did not change appreciably with the temperature under our experimental conditions. Hence, edge dislocations may not necessarily contribute to the FCD alignment.

## 4 Discussion

Three characteristic times observed in our stress-quench experiment have been attributed to the climb of edge dislocations, the FCD formation, and the alignment of FCDs, respectively. The slowing down behavior of $\tau_1$ and $\tau_2$ in the vicinity of $T_{SN}$ suggests that dislocation unbinding affects the climb motion and FCD formation.

In Fig. 10, a possible layer flipping scenario is illustrated. During stress-quenching from the $SmA_{II}$ to $SmA_I$ phases, the birefringence dramatically reduces on a time scale comparable to the first mode, indicating that the layer flips from the perpendicular to parallel orientation. The initial perpendicular orientation becomes unstable under low stress. The resulting large amplitude undulation induces a state like (b). The flow then encourages the layers to disassemble along the gradient direction, as illustrated in (c). The layers can reconnect in the neutral (vorticity) direction to form edge dislocations as drawn in the upper section of (d). Partially merged edge defects with opposite Burgers vectors, as illustrated in the lower section of (d), become oily streaks.[30] As shown in Fig. 4, $\tau_1$ behaves similarly regardless when the initial state $\sigma_i$ corresponds to $SmA_I$ or $SmA_{II}$. Hence, the layer-flipping process (Fig. 10(a)–(c)) should occur more rapidly than the defect climb process discussed earlier.

As argued before, undulation instability leads to edge dislocation when the smectic layer with parallel orientation undergoes the dilation deformation under shear flow.[32–35] Elementary edge dislocations may transform into FCDs to reduce the core energy.[26,28,30,32,36] Hence, the creation of edge dislocations is essential for structure formation in the smectic phase. Under shear stress, edge dislocations undergoing climb motion influence the shear rate depending on the mobility $b$ of the dislocation.[27,37] Oswald and Kleman studied the collective climb motion of edge dislocations under compression in Grandjean-Cano wedge with an angle $\alpha$.[34] They argued that, when the smectic sample is slightly compressed, the stress relaxes due to the cooperative climb motion of dislocations with a characteristic time

$$\tau_{\mathrm{climb}} \simeq \frac{d}{B\alpha b}. \tag{3}$$

Here $d$ is the sample thickness and $B$ is the layer compression modulus. At high defect densities, $d$ can be replaced by the FCD size. Using typical values of $d \simeq 10\ \mu m$, $B \simeq 10^6$ Pa,[38,39] $\sigma = 0.017$ rad, and $b \simeq 10^{-8}\ m^2\ s\ kg^{-1}$, we obtain $\tau_{\mathrm{climb}} \simeq 0.1$ s, which is roughly consistent with the experimental value $\tau_1$ of the first mode (see Fig. 4).

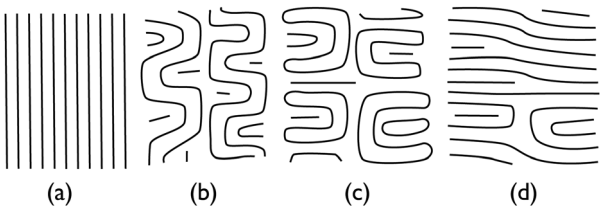


Fig. 10 Proposed layer-flipping scenario. Horizontal and vertical axes are the directions of vorticity and velocity gradient, respectively. (a) Initially, layers are perpendicularly oriented in the $SmA_{II}$ phase. (b) Layers destabilize and undulate with large amplitude. (c) Layers disassemble along the velocity gradient direction to allow for an easier flow. (d) Layers reconnect in the vorticity direction. The top section shows well-merged edge dislocations, and the lower section illustrates a cross-section of an oily streak.

One might also consider the contribution of the layer undulation mode to the first mode $\tau_1$. The typical relaxation time of the undulation mode is given by[40]

$$\tau_{\mathrm{und}} \simeq \frac{\eta_3}{Kq^2}, \tag{4}$$

where $\eta_3$ is the in-plane viscosity, $K$ the curvature elastic modulus, and $q$ the wavenumber of the undulation. Typical values of $\eta_3 \simeq 0.1$ Pa s, $K \simeq 10^{-11}$–$10^{-12}$ N,[27,41] and $q \simeq 10^5\ m^{-1}$ (corresponding to the FCD size) yields $\tau_{\mathrm{und}} \simeq 1$ s, again comparable to $\tau_1$. As observed for $\tau_1$, the undulation time $\tau_{\mathrm{und}}$ is also expected to increase as $T_{SN}$ is approached. However, typical $\tau_{\mathrm{und}}$ values are of the order of millisecond.[42] This means that evaluating $q$ from the FCD size (10 μm) is not justified. Hence, we attribute $\tau_1$ to the edge climb motion rather than the layer undulation mode.

As previously reported, FCDs are formed under shear flow.[1,9] Lu *et al.* theoretically explained the shear-thinning mechanism by the creation–annihilation dynamics of the dislocation loops.[7] In our earlier study, we found that the SN-transition, which is driven by dislocation unbinding, affects the mechanical property. We reported that the average FCD size varies as $L \sim \dot{\gamma}^{-0.2}\varepsilon^{-0.5}$.[10] Although $L$ has not been theoretically predicted, Meyer *et al.* argued that the distance between edge dislocations behaves as $\sim\dot{\gamma}^{-0.2}$.[5,6] On the other hand, the unbinding transition theory[17] predicts that the size of the dislocation loop depends on the reduced temperature as $\sim\varepsilon^{-0.5}$. Hence, we expect that the FCD size is determined by unbinding properties of the dislocation loop, which characterize $\tau_2$. Very recently, Chatterjee and Anna studied the effects of shear and dilation flows on toroidal and parabolic FCD formations.[11,12] They showed that the critical dilation required for parabolic FCD formation increases under shear flow because such flow annihilates dislocations.

The smectic phase with FCDs exhibits the yield stress in the order of $\sigma_y \simeq 10^{-2}$–$10^0$ Pa.[1,9] The yield stress originates from the line tension of oily streaks that depends on its internal structure. According to Boltenhagen *et al.*, the main contribution to the line tension $\Gamma$ is the layer compression energy, given by[30]

$$\Gamma \simeq Bd^2\left(\frac{e}{\sqrt{1-e^2}} - \frac{a}{d}\right), \tag{5}$$

where $e$ and $a$ are eccentricity and major elliptic axis of a FCD, respectively. Our FCD measurements yield $e \simeq 0.6$ and $a \simeq 10$–$100\ \mu m$. Using the previously mentioned values, we estimate $\Gamma \simeq 10^{-2}$ Pa, which is roughly consistent with the experimentally observed yield stress.[9] We showed that the characteristic time $\tau_3$ increases as $\sigma_f$ approaches $\sigma_y$, whereby the shear rate decreases to zero. Hence, we consider that $\tau_3$ is determined by the mechanical balance between the applied stress $\sigma_f$ and the line tension of the oily streak $\Gamma$.

# 5 Conclusion

We studied the dynamics of FCD formation in the smectic phase by performing stress-quench experiments on the thermotropic liquid crystal 8CB. In particular, we investigated both

 

the rheological response and the structural evolution as the system transforms from the $SmA_{II}$ phase under high shear stress to the $SmA_{I}$ phase under low shear stress. We identified three distinct characteristic times. The first mode is attributed to the climb motion of edge dislocations created when layers flip from perpendicular to parallel orientations. The second mode corresponds to the FCD formation. Both of these decay modes also occur when the system is quenched within the $SmA_{I}$ phase. The slowing down of the characteristic times $\tau_1$ and $\tau_2$ in the vicinity of the SN-transition indicates that the dislocation unbinding influences the formation of edge dislocations. The third mode originates from the alignment of FCDs into oily streaks. Such a FCD alignment is determined by the balance between the shear stress and the line tension of the oily streak.

## Acknowledgements

Both SF and SK acknowledge support from the Grand-in-Aid for Scientific Research (B), grant no. 25287107 from the Ministry of Education, Culture, Sports, Science and Technology (MEXT) of Japan. SF thanks T. Takahashi, H. Orihara and Anton Paar Co. Ltd for the use of their rheometer and the microscopy devices. SK would like to further acknowledge support from the Grant-in-Aid for Scientific Research on Innovative Areas "Fluctuation & Structure" (grant no. 25103010), grant no. 24540439 from the MEXT of Japan, and the JSPS Core-to-Core Program "International research network for non-equilibrium dynamics of soft matter".

## References

1 R. G. Horn and M. Kleman, *Ann. Phys.*, 1978, **3**, 229–234.
2 R. G. Larson, *The Structure and Rheology of Complex Fluids*, Oxford University Press, Oxford and New York, 1999.
3 R. H. Colby, C. K. Ober, J. R. Gillmor, R. W. Connelly, T. Duong, G. Galli and M. Laus, *Rheol. Acta*, 1997, **36**, 498–504.
4 R. H. Colby, L. M. Nentwich, S. R. Clingman and C. K. Ober, *Europhys. Lett.*, 2001, **54**, 269–274.
5 C. Meyer, S. Asnacios, C. Bourgaux and M. Kleman, *Rheol. Acta*, 2000, **39**, 223–233.
6 C. Meyer, S. Asnacios and M. Kleman, *Eur. Phys. J. E*, 2001, **6**, 245–253.
7 C.-Y. D. Lu, P. Chen, Y. Ishii, S. Komura and T. Kato, *Eur. Phys. J. E*, 2008, **25**, 91–101.
8 O. Henrich, K. Stratford, D. Marenduzzo, P. V. Coveney and M. E. Cates, *Soft Matter*, 2012, **8**, 3817–3831.
9 S. Fujii, Y. Ishii, S. Komura and C.-Y. D. Lu, *EPL*, 2010, **90**, 64001.
10 S. Fujii, S. Komura, Y. Ishii and C.-Y. D. Lu, *J. Phys.: Condens. Matter*, 2011, **23**, 235105.
11 S. Chatterjee and S. L. Anna, *Soft Matter*, 2012, **8**, 2698–2705.
12 S. Chatterjee and S. L. Anna, *Phys. Rev. E: Stat., Nonlinear, Soft Matter Phys.*, 2012, **85**, 011701.
13 O. Henrich, K. Stratford, D. Marenduzzo, P. V. Coveney and M. E. Cates, *Soft Matter*, 2013, **9**, 10243–10256.
14 P. Moreau, L. Navailles, J. Giermanska-Kahn, O. Mondain-Monval, F. Nallet and D. Roux, *Europhys. Lett.*, 2006, **73**, 49–54.
15 P. Panizza, P. Archambault and D. Roux, *J. Phys. II*, 1995, **5**, 303–311.
16 C. R. Safinya, E. B. Sirota and R. J. Plano, *Phys. Rev. Lett.*, 1991, **66**, 1986–1989.
17 W. Helfrich, *J. Phys.*, 1978, **39**, 1199–1208.
18 M. Imai, A. Saeki, T. Teramoto, A. Kawaguchi, K. Nakaya, T. Kato and K. Ito, *J. Chem. Phys.*, 2001, **115**, 10525–10532.
19 M. Vasudevan, E. Buse, D. Lu, H. Krishna, R. Kalyanaraman, A. Q. Shen, B. Khomami and R. Sureshkumar, *Nat. Mater.*, 2010, **9**, 436–441.
20 M.-A. Fardin and S. Lerouge, *Eur. Phys. J. E*, 2012, **35**, 91.
21 D. Derks, D. G. A. L. Aarts, D. Bonn and A. Imhof, *J. Phys.: Condens. Matter*, 2008, **20**, 404208.
22 O. Diat, F. Nallet and D. Roux, *J. Phys. II*, 1993, **3**, 1427–1452.
23 B. Medronho, S. Fujii, W. Richtering, M. G. Miguel and U. Olsson, *Colloid Polym. Sci.*, 2005, **284**, 317–321.
24 S. Fujii and W. Richtering, *Soft Matter*, 2013, **9**, 5391–5400.
25 M. Kleman and O. D. Lavrentovich, *Soft Matter Physics: An Introduction*, Springer, New York, 2003.
26 J. Rault, *Philos. Mag.*, 1976, **34**, 753–765.
27 P. Oswald and P. Pieranski, *Smectic and Columner Liquid Crystals*, Taylor & Francis, Boca Raton, 2006.
28 C. E. Williams and M. Kleman, *J. Phys., Colloq.*, 1975, **36**, C1-315.
29 P. Oswald and M. Kleman, *J. Phys.*, 1984, **45**, L319–L328.
30 P. Boltenhagen, O. Lavrentvich and M. Kleman, *J. Phys. II*, 1991, **1**, 1233–1252.
31 M. Rex and H. Löwen, *Phys. Rev. E: Stat., Nonlinear, Soft Matter Phys.*, 2007, **75**, 051402.
32 P. Oswald and M. Allain, *J. Phys.*, 1985, **46**, 831–838.
33 P. Oswald and S. I. Ben-Abrahm, *J. Phys.*, 1982, **43**, 1193–1197.
34 P. Oswald and M. Kleman, *J. Phys.*, 1982, **43**, L411–L415.
35 R. Bruinsma and Y. Rabin, *Phys. Rev. A*, 1992, **45**, 994–1008.
36 C. S. Rosenblatt, R. Pindak, N. A. Clark and R. B. Meyer, *J. Phys.*, 1977, **38**, 1105–1115.
37 R. Ribotta and G. Durand, *J. Phys.*, 1977, **38**, 179–204.
38 M. Benzekri, J. P. Marcerou, H. T. Nguyen and J. C. Rouillon, *Phys. Rev. B: Condens. Matter Mater. Phys.*, 1992, **41**, 9032–9037.
39 M. Benzekri, T. Claverie, J. P. Marcerou and J. C. Rouillon, *Phys. Rev. Lett.*, 1992, **68**, 2480–2483.
40 P. G. De Gennes and J. Prost, *The Physics of Liquid Crystals*, Clarendon Press, New York, 1993.
41 A. Zywocinski, F. Picano, P. Oswald and J. C. Geminard, *Phys. Rev. E: Stat. Phys., Plasmas, Fluids, Relat. Interdiscip. Top.*, 2000, **62**, 8133–8140.
42 R. Ribotta, D. Salin and G. Durand, *Phys. Rev. Lett.*, 1974, **32**, 6–9.